12th international symposium on Applications of Laser Techniques to Fluid Mechanics, Lisbon, July 2004, CD-ROM publication, 30-2.

Coaxial Jet Control for Lifted Flame Stabilization with Arrayed Miniature Actuators

by

N. Kurimoto[(1)], Y. Suzuki[(2)] and N. Kasagi[(3)]

Department of Mechanical Engineering, The University of Tokyo

7-3-1 Hongo Bunkyo-ku, Tokyo, 113-8656; Japan

[(1)]E-Mail: kurimoto@thtlab.t.u-tokyo.ac.jp

[(2)]E-Mail: ysuzuki@thtlab.t.u-tokyo.ac.jp

[(3)]E-Mail: kasagi@thtlab.t.u-tokyo.ac.jp

ABSTRACT

Active control of a lifted flame is investigated using a coaxial nozzle with magnetic flap actuators arranged on the inner periphery of the annular nozzle. Near-field vortical structures of the methane/air coaxial jet are manipulated by introducing disturbances directly to the initial shear layer. Through the manipulation, we can improve flame stability and flexibly control the liftoff height. It is found that the large-scale vortical structures play a dominant role in the flame stabilization, and its spatio-temporal evolution is examined with the aid of PIV and LIF to elucidate the control mechanism. By introducing flap motion driven with a saw-wave signal, we can force the outer shear layer to roll up into strong vortices in synchronization with the flaps. When the flapping Strouhal number is unity, the lifted flame is anchored at $x/D_o \sim 1.5$. The strong vortices induced by the flaps produce a blob of flammable mixture, which has velocity smaller than the flame speed. The possible stabilization mechanism is that the time period of the premixture supply is balanced with the consumption time of the premixture at the flame base. On the other hand, when the jet is manipulated by a square-wave signal, the lifted flame is located stably at $x/D_o \sim 4$, which is downstream of the inner potential core. It is found that vortical structures in the shear layers break into turbulence close to the nozzle exit. The possible mechanism of the flame stabilization is that the flame propagating upstream is undisturbed due to the absence of intermittent passage of large-scale vortices.

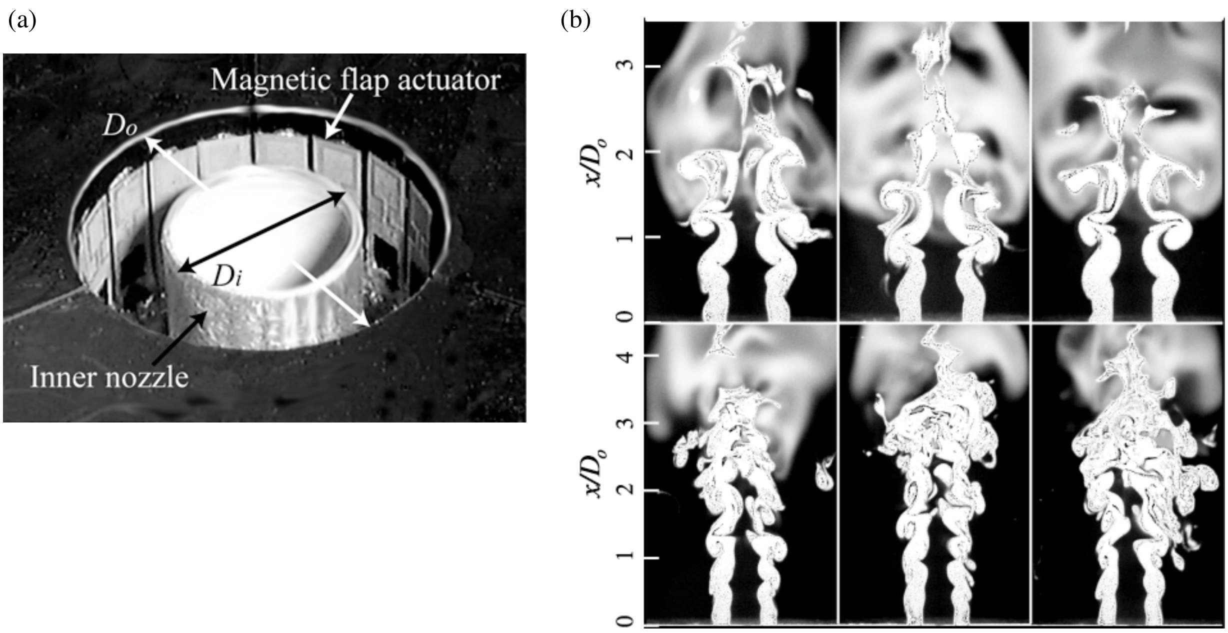

Fig. 1. a) Coaxial nozzle equipped with eighteen magnetic flap actuators.
b) Controlled lifted flames by the flap motion driven with the saw- or the square-wave signals.

1. INTRODUCTION

Lifted flame is a typical form of flame in industrial combustors. Flamed fuel jet surrounded by an annular air flow forms a diffusion flame. If the velocity of fuel and/or air flow is larger than a critical value, the flame cannot be held at the burner rim, so that it should be lifted. The flame base is anchored at a certain downstream distance if the air and fuel velocities are smaller than the blowoff limits. It is of practical importance in designing industrial burners to predict the flame characteristics such as liftoff heights and liftoff/blowoff conditions. Many studies on lifted flames have focused on estimating these features through modeling the stabilization mechanism (Pitts, 1988). For instance, Vanquickenborne & Triggelen (1966) hypothesize that the fuel is well premixed with the air at the upstream and the turbulent burning velocity balances with the flow velocity at the flame base. Based on these assumptions, they successfully derive an empirical relation between the turbulent burning velocity and parameters of turbulence. On the other hand, Peters & Williams (1983) assume that the liftoff process is controlled by the quenching of laminar diffusion flamelets, which is dominated by a local scalar dissipation rate. They verify their assumption by estimating the liftoff heights with the scalar dissipation rate calculated. Recently, it is reported that fuel and air are partially premixed upstream of the flame base and that a laminar triple flame is dominant in the flame stabilization mechanism (Vervisch, 2000). Muniz & Mungal (1997) measured the instantaneous, two-dimensional velocity field at the lifted flame base by using PIV (particle image velocimetry). They observed instantaneous flame fronts and velocity profiles, which are similar to those predicted by numerical simulations of the triple flames. They also revealed that the lifted flame certainly blows off if the velocity of the surrounding air flow is more than three times larger than the laminar burning velocity.

In addition to these studies, some researchers have tried to improve the flame stability through intensifying orderly jet structures with acoustic excitation. Chao *et al.* (1992) excited a propane/air premixed lifted flame by adding axial disturbances with a loud speaker. They showed that the induced vortices made the flame base anchored near the nozzle exit. Chao *et al.* (2000) arranged eight piezoelectric actuators around a nozzle exit in order to add helical-mode disturbances to the jet shear layer. They showed that the helical-mode excitation intensified one of the streamwise vortices in the jet braid region, which played an important role in the flame stabilization. It is concluded that the controlled flame base is inclined to the nozzle by the streamwise vortex which provides an additional path for the upstream flame propagation. However, any attempt to control the flame position flexibly has not been made.

Recently, smart control of turbulent shear flows has attracted much attention. The development of MEMS (Micro electro-mechanical Systems) technology make it possible to fabricate miniature actuators, which are small enough to impose direct control input on the shear layers. Various kinds of miniature actuators have been developed and applied to the control systems (Gad-el-hak, 2002). In particular, Suzuki *et al.* (2004) developed miniature magnetic flap actuators and arranged eighteen flaps on the inner wall of a round nozzle to control the near-field vortical structures, and they created a furcating jet by modulating the azimuthal phase of the disturbances introduced into the jet shear layer.

The objective of the present study is to develop an active control scheme for the lifted flame, with which the flame position can be controlled flexibly. For this purpose, we introduce an axisymmetric coaxial nozzle equipped with flap actuators. In order to examine the control mechanism in terms of large-scale vortical structures, we employ two-components particle image velocimetry (2C-PIV) and laser-induced fluorescence method (LIF) with acetone vapor as a tracer.

2. EXPERIMENTAL SETUP

2.1 Coaxial nozzle and magnetic flap actuator

Axisymmetric coaxial jet nozzle employed in the present study is shown in Fig. 2. The annular nozzle consists of a convergent nozzle with a contraction area ratio of 42 and the internal diameter D_o is 20 mm at the exit. The inner nozzle consists of a straight tube with a wall thickness of 0.3 mm. The inner diameter ratio □ (= D_o/D_i) is 2. Eighteen flap actuators (Suzuki *et al.*, 2004) are arranged on the inner wall of the outer nozzle lip, which cover 86% of the circumference. In the present study, all flaps are driven in phase. According to Dahm *et al.* (1992) and Rehab *et al.* (1997), the near-field vortical structures of coaxial jets are dominated by the vortices emerging in the outer shear layer when the velocity ratio is larger than unity. Therefore, we add the control input into the outer shear layer in order to manipulate the vortical structures effectively.

The miniature flap actuator is made of a copper plated polyimide film of 9 mm in length and 3 mm in width. Each thickness of the polyimde and copper layer is 35 μm. A coil-shaped copper circuit is left on the flap after several MEMS processes. When an electric current is applied to the copper coil, the flap is elastically bent by the magnetic force generated between the coil and a cylindrical permanent magnet embedded in the nozzle wall. The flap is driven by an alternating current, which is generated by amplified voltage signals from a function generator. Four kinds of voltage signals (sinusoidal-, triangle-, saw- and square-wave) were examined in a preliminary experiment in order to find the effective flapping motion. In the present study, we focus on the square-wave and saw-wave signals, since they have produced significant effects on the development of shear layer.

The flap movement is measured with a laser displacement meter (Keyence, LC-2440). The measurement point is located at 1.5 mm from the free end of the flap. Figure 3 shows the time response when it is driven with the saw- and square-wave voltage signals at 95 Hz. When it is driven with the saw-wave signal, the head of the flap starts to lift gradually following the wave (Fig. 3a). It includes the damping oscillation, but the amplitude is small. Right after it reaches the maximum displacement of 0.3 mm, it is quickly pulled back to the initial position following the trailing edge of the signal. On the other hand, when it is driven with the square-wave signal, the flap is quickly repelled upward following the initial rise of the signal (Fig. 3b). After reaching the maximum displacement of 0.6 mm, it exhibits the damping oscillation at its natural frequency of 310 Hz. The oscillation lasts until the flap is pulled back to the initial position. The power consumption of each mode is 0.5 and 0.2 W respectively for the square- and saw-wave signals, and they are negligible compared to a 3.5 kW burn rate in the present study.

2.2 Flow facility

Schematic of the experimental setup is shown in Fig. 4. The central and annular flows are methane and air, respectively. The methane is supplied from a compressed gas container and forms a fully developed flow in a straight tube at 1 m from the inlet. The air is supplied from a compressor and introduced into a plenum chamber with a honeycomb and several meshes. The uniform air flow becomes an annular jet through the convergent nozzle with the flap actuators at the exit. Flow rates of the both streams are independently managed by two mass flow meters (Yamatake, CMQ series). The coaxial jet is discharged vertically into the static ambient air, which is surrounded by four plates. Each plate has a quartz window, which provides optical access for a laser sheet and image acquisition. The test section is 1000 mm in height with a square cross section of 560 x 560 mm^2. Hereafter, the cylindrical coordinate system is employed with x denoting the streamwise direction, while r and θ are the radial and azimuthal directions, respectively.

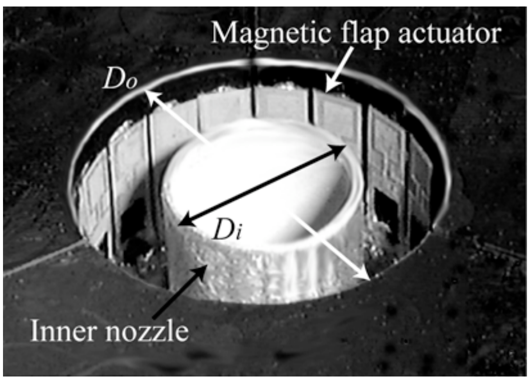

Fig. 2. Coaxial nozzle equipped with eighteen magnetic actuators.

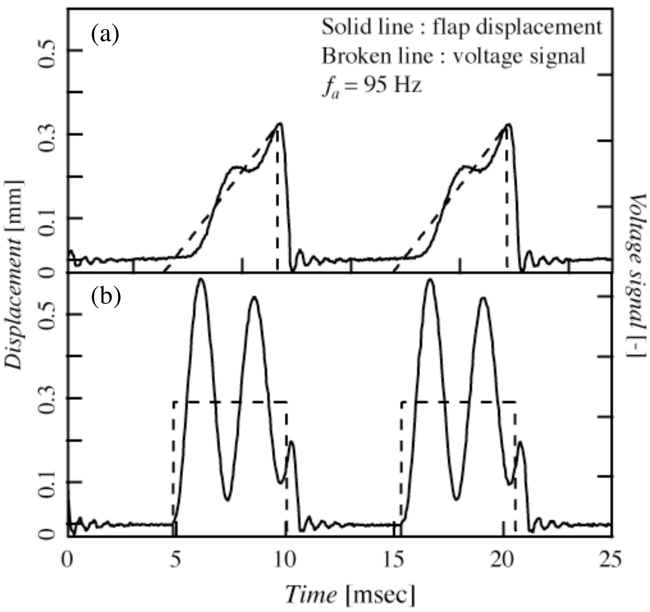

Fig. 3. Time response of an magnetic flap actuator to the square and saw-wave voltage signal.
a) saw-wave voltage signal control
b) square-wave voltage signal control

2.3 Particle image velocimetry

Two-component particle image velocimetry (2C-PIV) is employed for velocity measurement. The inner and outer jets are seeded with silica particles (d_p = 1.2 mm, ρ_p = 215 kg/m3). The particle relaxation time τ_p is approximately 1 μs (Melling, 1997), which is much smaller than the Kolmogorov time scale τ_k ~ 222 μs estimated by $D_o^2 Re^{-3/2}/\nu_{air}$. The seeding system consists of a vessel filled with the particles, which are agitated and suspended by a magnetic stirrer, and a part of the inner and outer flows goes through the system to keep seeding rate constant.

A double-pulsed Nd: YAG laser (THALES, SAGA PIV20, 400 mJ/pulse at 532 nm) is employed for the light source. The laser beam is formed into a sheet (~ 1 mm thick) through several cylindrical lenses and introduced into the test section. The time interval of the laser pulses is chosen as 50 μs in order to minimize the unwanted effect of the velocity gradient in the shear layer (Kean & Adrian, 1992). The yield of the velocity vectors thus obtained is more than 95 %. Particle images are captured by a frame-straddling CCD camera (Lavision, FlowMaster3, 1280 x 1024 pixels) equipped with a Nikon 50 mm f/11 lens. The field of view is 56 x 45 mm^2. Commercial software (Lavision, Davis 6) is used to calculate the average particle displacement in an interrogation area with a cross-correlation technique. The size of the interrogation area is 32 x 32 pixels^2, which correspond to a physical dimension of 1.4 x 1.4 mm^2. The images are processed to yield 80 x 64 vectors with 50 % overlap in each direction. Suspicious vectors having low correlation ratio between the first and second peaks are rejected (Kean & Adrian, 1990). The threshold is chosen as 1.3. The uncertainty interval estimated at 95 % coverage by the method of ANSI/ASME PTC (1985) is 7 % for the instantaneous velocity, $U_{m,o}$ = 1.84 m/s, which corresponds to the bulk mean velocity of the annular jet. The precision index and bias limit are 2 % and 6 %, respectively.

2.4 Laser-induced fluorescence

Scalar mixing process is investigated through a planar laser-induced fluorescence method (PLIF). The inner methane flow is seeded with acetone vapor by bubbling the career gas into a liquid acetone container (Lozano *et al.*, 1992). Stable seeding is achieved once thermal equilibrium is reached. The acetone temperature is approximately 291 K, which corresponds to partial pressure of 2.4 x 10^4 Pa. Acetone vapor is excited by a frequency-doubled pulsed dye laser, which is pumped by a doubled Nd:YAG laser (Lamda Physik, SCANmate). Rhodamine 6G dye is chosen to produce 283 nm UV light pulses of 10 mJ/pulse. The laser beam is introduced into the test section through a quartz window and formed into a laser sheet having 0.4 mm in thickness (1.4 mJ/cm intensity). An image-intensified CCD camera (LaVision, Flamestar2; 576 x 384 pixels) is employed for image acquisition. The ICCD camera is equipped with a 100 mm UV lens as well as a low-pass optical filter (cutoff wavelength = 295 nm) to eliminate the Mie scattering of the laser sheet from dust particles. The field of view is set to be 60 x 40 mm^2. In order to reduce the effect of shot noise,

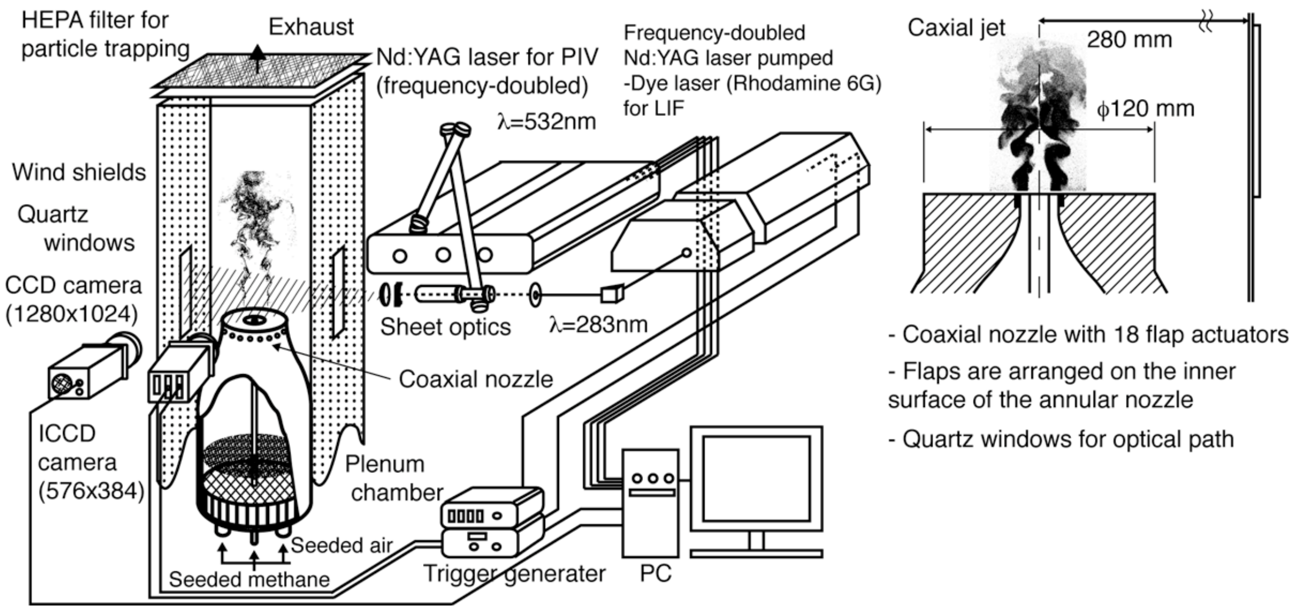

Fig. 4. Schematic view of the experimental setup.

fluorescence signals in a subregion of 4 x 4 pixels^2 are ensemble-averaged, which results in the spatial resolution of 0.4 mm^2. The Kolmogorov length scale is estimated to be $D_oRe^{-3/4}$ = 0.06 μm, which is somewhat smaller than the spatial resolution of the concentration measurement.

Fluorescent intensity at each pixel is converted to the instantaneous relative scalar concentration by

$$\frac{\tilde{c}}{\tilde{c}_o} = \frac{\left[I_{FL}(x_n,r_n) - I_{BG}(x_n,r_n)\right] / \left[I_{ref}(x_n) - I_{BG}(x_n,r_n)\right]}{\left\langle \left[I_{FL}(x_n,r_n) - I_{BG}(x_n,r_n)\right] / \left[I_{ref}(x_n) - I_{BG}(x_n,r_n)\right] \right\rangle_{core}}, \qquad (1)$$

where I_{FL}, I_{ref}, and I_{BG} are respectively the raw fluorescent intensity, the reference image intensity and the background intensity. The bracket $< >_{core}$ represents a spatial average in the jet potential core. By Eq. (1), spatial variation of the laser pulse energy and pulse-to-pulse variation are compensated. Intensity of each laser pulse is evaluated through averaging the fluorescence signals in the potential core. The reference image for the correction of the spatial is taken by introducing laser sheet into a quartz container filled with acetone vapor. Note that the linearity of the fluorescent intensity versus the acetone concentration and incident light intensity is ensured.

3. COLD JET CONTROL

3.1 Visualization

Instantaneous LIF images of the natural and controlled cold jets are shown in Fig. 5, where acetone vapor is separately seeded in the inner or outer flow. The bulk mean velocities of the inner and outer flows are respectively $U_{m,i}$ = 1.2 m/s and $U_{m,o}$ = 1.8 m/s. For a methane/air jet, the present flow condition corresponds to a 3.5 kW diffusion flame. The Reynolds number Re (= $U_{m,o}D_o/\nu_o$) is 2.4 x 10^3 and the momentum flux ratio m (= $\rho_oU_{m,o}^2/\rho_iU_{m,i}^2$) is 4. As shown in Figs. 5ab, the inner and outer shear layers in the natural jet start to roll up into large-scale vortices at x/D_o ~ 2 through the column-mode instability (Hussain & Zaman, 1981). The preferred-mode frequency f_p of the vortex shedding was 57 Hz, which corresponds to the Strouhal number St_p (= $f_pD_o/U_{m,o}$) of 0.62.

On the other hand, in the controlled jet with the saw-wave signal (Case 1), the outer shear layer is forced to roll up into large-scale vortices in phase with the flap motion, and the vortices pinch off the inner jet significantly (Figs. 5cd). Since the vortex shedding frequency f_v is the same as the flapping frequency f_a, which is much smaller than f_p, the vortex shedding is independent of the column mode instability. In the present study, f_a is set to be 95 Hz ($St_a = f_aD_o/U_{m,o}$ = 1), which is the optimum frequency for flame stabilization. Figures 5ef show the controlled jet with the square-wave signal at the same flapping frequency (Case 2). Unlike Case 1, the large-scale vortical structures are not observed in the outer shear layer, although the flapping frequency is the same.

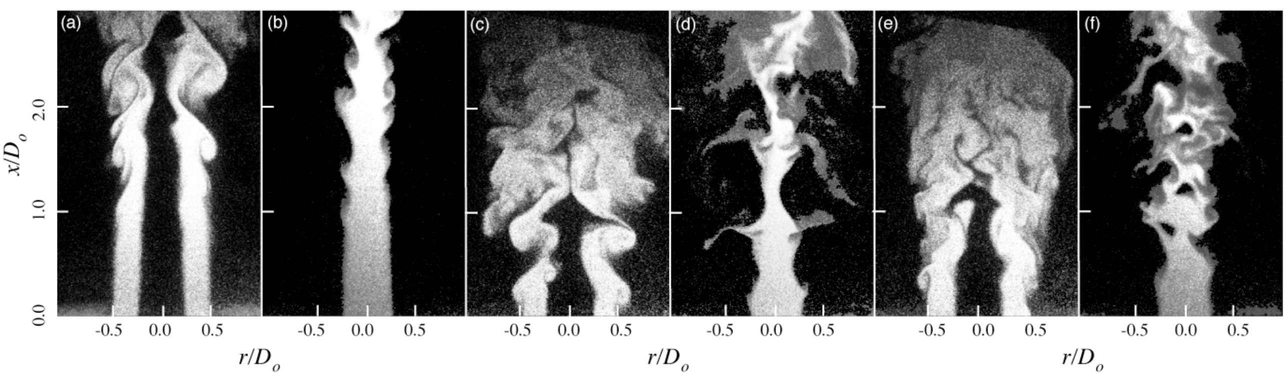

Fig. 5. Instantaneous images of the natural and controlled coaxial jets.
a), b) Natural jets.
c), d) Controlled jet by the flap motion driven with the saw-wave voltage signal at St_a = 1.0 (Case 1)
e), f) Controlled jet by the flap motion driven with the square -wave voltage signal at St_a = 1.0 (Case 2)

3.2 Vortical structures and mass transfer

In the present study, phase-averaged field is employed to examine the vortical structures in detail; the instantaneous velocity $\tilde{u}$ is decomposed into $(\bar{u} + u_{\square} + u\square)$, where $\bar{u}$, $u_{\square}$ and $u\square$ respectively correspond to the mean, phase-averaged and fluctuating velocities. Figure 6 shows $\tilde{u}$, $(u_{\square} + u\square)$, $\sqrt{\overline{u\square^2}}$ and $u_{\square}$ in the controlled jet. In addition, contours of the rich and lean flammable limits of fuel/air mixture fraction, i.e., $(\bar{Z} + Z_{\square})$ = 0.091 and 0.026, are also depicted on Fig. 6dh. The mixture fraction is estimated from the LIF images of cold jets, where the acetone vapor is seeded into the inner methane flow. Based on an assumption that the distribution of the acetone vapor equals that of the methane, the mixture fraction is calculated as follows:

$$\tilde{Z} = \square_f M_f \Big/ \left[\square_f M_f + \left(1 \square \square_f\right) M_a \right], \tag{2}$$

where M_f and M_a are respectively the molecular weights of methane and air, while $\square_f$ is the concentration of the acetone vapor nondimensionalized by its concentration at the potential core.

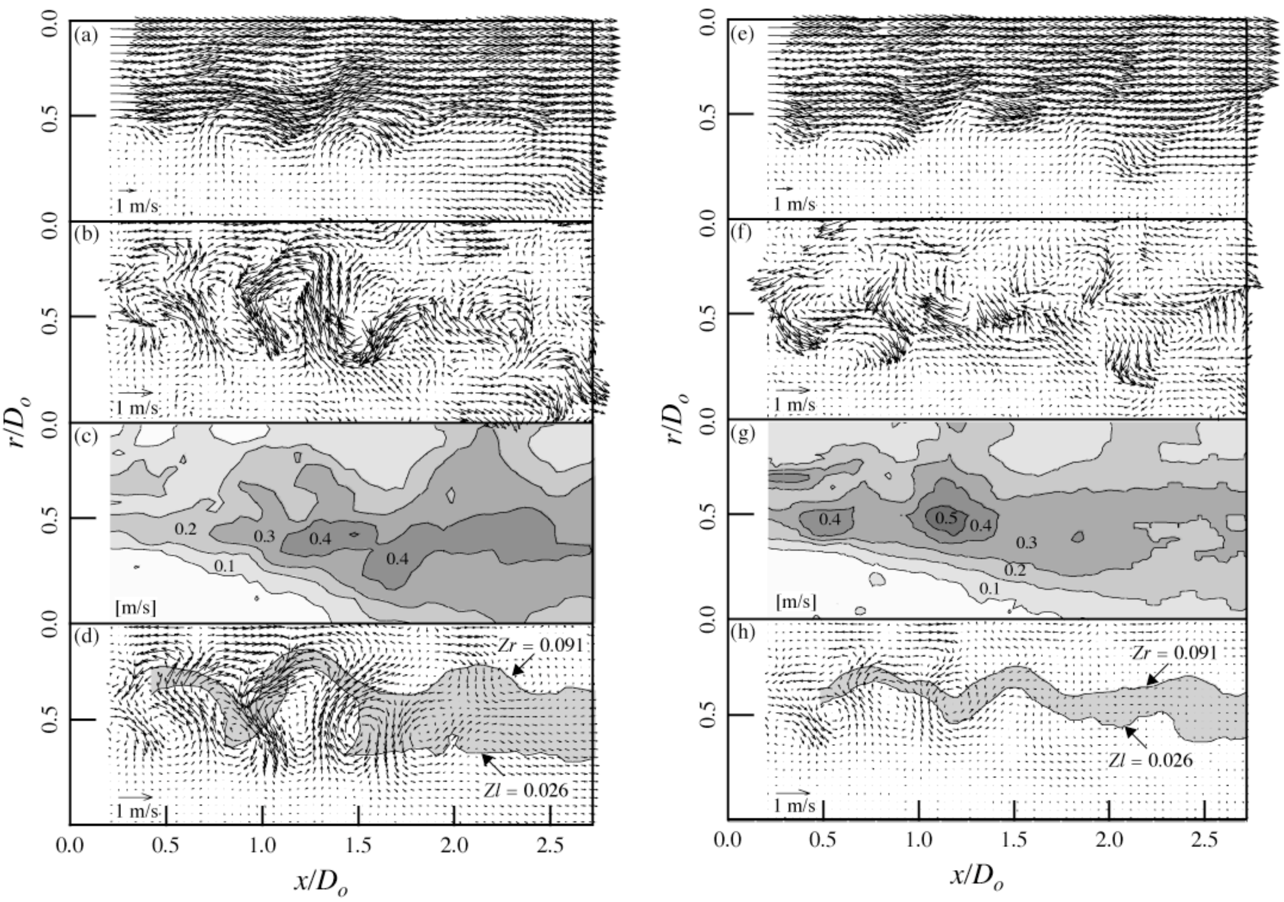

Fig. 6. Velocity and mixture fraction of the controlled coaxial jets with the saw- and square-wave siganls.

a), e) Instantaneous velocity vectors, $\tilde{u}$

b), f) Phase-averaged velocity vectors plus instantaneous fluctuating vectors, $(u_{\square} + u\square)$

c), g) RMS value of the fluctuating component, $\sqrt{\overline{u\square^2}}$

d), h) Phase-averaged velocity vectors, $u_{\square}$*, and contours of the rich and lean flammable limits of the mixture fraction, i.e.,* $(\bar{Z} + Z_{\square})$ *= 0.091 and 0.026, respectively*

As shown in Figs. 6ab, in Case 1, large-scale vortices are periodically produced by the flap motion and densely populated near the nozzle exit. The magnitude of those vortices are strong and remain axisymmetric at $x/D_o < 1.5$, while they break down into turbulence further downstream. Therefore, $\sqrt{\overline{u'^2}}$ shown in Fig. 6c is small near the nozzle exit, while it increases downstream until reaching a peak at $x/D_o = 1 \sim 1.5$. Separate flow visualization in a preliminary experiment shows that an intense vortex is emerged in the outer shear layer at the downward motion of the flap. The large-scale vortex transports the inner fluid in the radial direction, and a kink in iso-contours of the concentration field is formed at the center of the primary vortex (Fig. 6d). The flammable mixture is located in the vortex at $x/D_o < 1.5$, while it is distributed extensively in the radial direction further downstream due to the vortex breakdown.

On the other hand, in Case 2, large-scale vortical structures are weaker than in Case 1, and break into turbulence near the nozzle exit. Therefore, $\sqrt{\overline{u'^2}}$ becomes large at $x/D_o \sim 0.5$. Because of the early breakdown of the vortices, radial transportation of the inner fluid is small, and the width of the flammable mixture is much smaller than that in Case 1.

4. LIFTED FLAME CONTROL

4.1 Flame observations

Instantaneous images of the natural and controlled lifted flames are shown in Fig. 7. The flow conditions are the same as those of the cold jets ($Re = U_{m,o}D_o/\nu_o = 2.4 \times 10^3$, $m = \rho_o U_{m,o}^2/\rho_i U_{m,i}^2 = 4$). The annular air flow is visualized using smoke, and the image is captured together with luminescence of the flame. As shown in Fig. 7a, the natural flame is located near the end of the inner potential core, where large-scale vortices emerge intermittently. The natural lifted flame is unstable and easily blows off. This is probably because the vortices emerging at the potential core end disturb the flame propagation significantly.

On the other hand, the controlled flames become stable for both Case 1 and Case 2. In Case 1, the large-scale vortices induced by the flaps are clearly observed near the flame base, and the flame is anchored at $x/D_o \sim 1.5$. The total flame length is approximately $15D_o$ (Fig. 7b). At the flame base, blue chemiluminescent emission is observed, while luminous flame with its length of $\sim 12D_o$ is observed downstream. These observations imply that partially premixed combustion is dominant at the flame base, while diffusion combustion prevails downstream. In Case 2, the flame is held at $x/D_o \sim 3.5$, which is further downstream of the inner potential core (Fig. 7c). The total flame length is approximately $10D_o$ and blue chemiluminescent emission is observed at the flame base with its length of $\sim 6D_o$. Therefore, partially premixed combustion should be dominant in the flame.

Figure 8 shows an instantaneous flame front and the streamwise velocity profiles in the controlled flames. The instantaneous flame front is estimated using an abrupt decrease in the particle density, indicating a thermal boundary between the hot and cold gas (Muniz & Mungal, 1997). For both Case 1 and Case 2, the leading edge flame is located near the boundary between the outer shear layer and the ambient fluid. In Case 1, the flame fronts are far from the jet axis at $x/D_o \sim 2$, implying that much amount of unburned fuel remains around the jet axis (Fig. 8a). The unburned fuel is likely to be consumed downstream as a diffusion flame, which is in accordance with the observation of the luminous flame at the downstream. In Case 2, since the flame fronts are close to the jet axis at $x/D_o \sim 4$, the flammable mixture is likely to be distributed near the jet axis (Fig. 8a). Therefore, partially premixed combustion is dominant in the flame, which is also consistent with the observation of the blue chemiluminescent emission at the flame base.

4.2 Blowoff limits

Figure 9 shows the maximum momentum flux ratio m for sustaining stable flame. The lifted flame is defined as stable when it is held at least for 3 minutes. In the natural flame, the blowoff limit is insensitive to Re, and it ranges from m = 1.5 to 2. On the other hand, in the controlled flames, the blowoff limit is significantly extended to larger m for $Re > 2.0 \times 10^3$. For example, for $Re = 2.4 \times 10^3$, the blowoff limit in Case 1 is approximately five times larger than that of the natural flame, while that of Case 2 is three times larger.

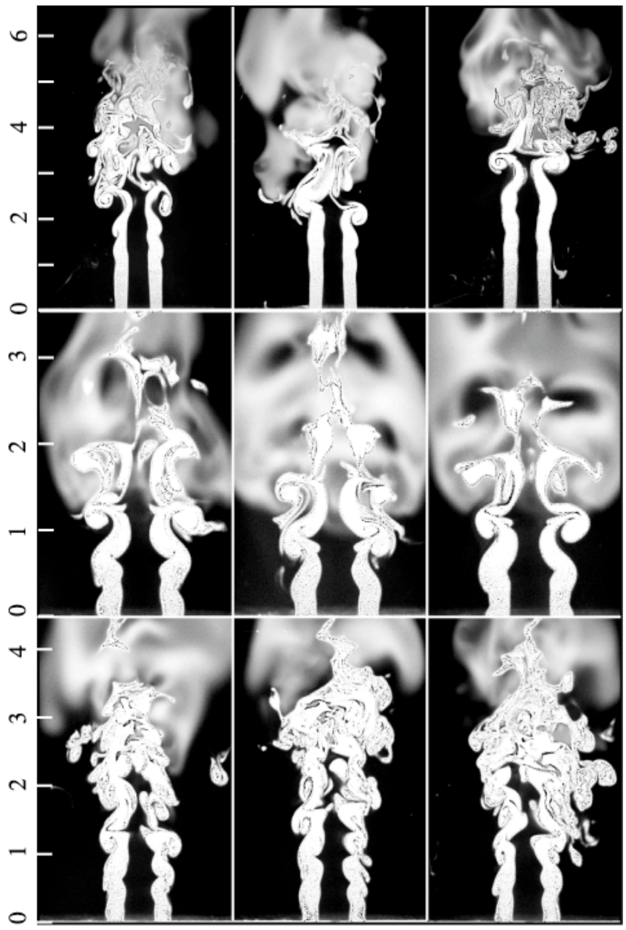

Fig. 7. Instantaneous images of the natural and controlled lifted flames.

a) Natural flame

b) Controlled flame with the saw-wave signal (Case 1)

c) Controlled flame with the square -wave signal (Case 2)

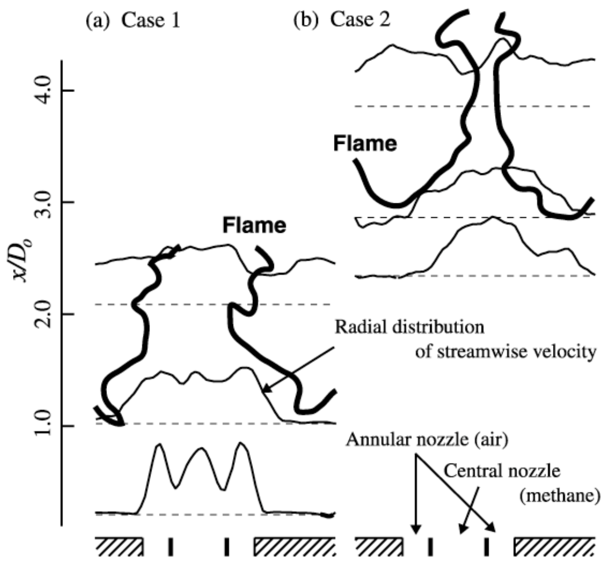

Fig. 8. Sketch of the instantaneous flames and distributions of the streamwise velocity.

a) Controlled flame in Case 1

b) Controlled flame in Case 2

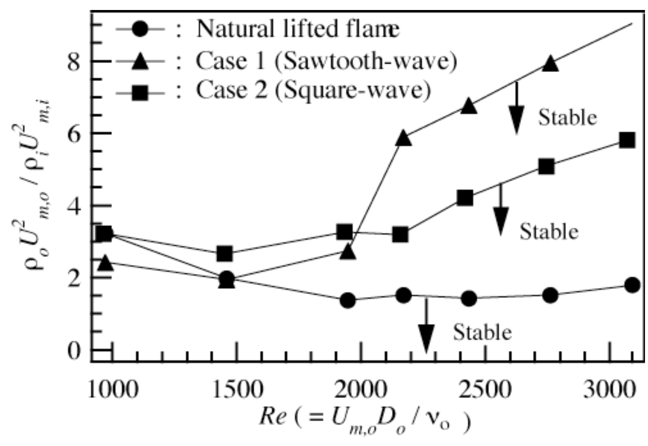

Fig. 9. Blowoff limits of the natural and controlled flames with $St_a = f_a D_o / U_{m,o}$ = 1.0.

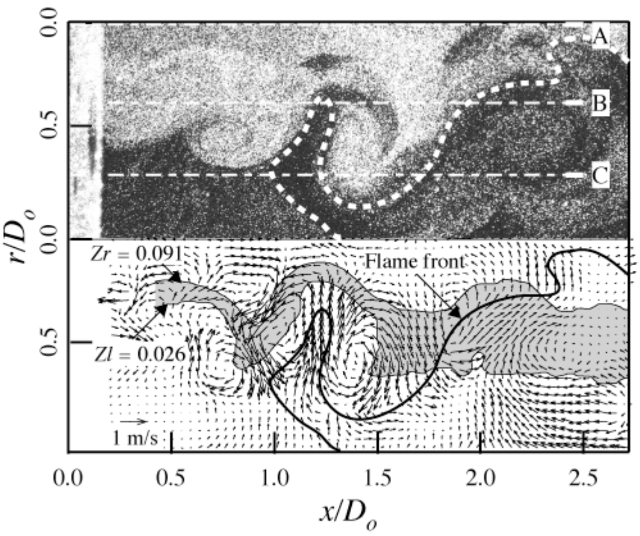

Fig. 10. Instantaneous particle images and the velocity, $(u_{\square} + u\square)$, for the controlled lifted flame in the case 1. Instantaneous thermal boundary and contours of the flammable limits in the mixture fraction, $(\overline{Z} + Z_{\square})$, are depicted in the figure.

4.3 Flame base structures for Case 1

A snap shot of the particle images and the velocity vectors $(u_{\square} + u\square)$ are shown in Fig. 10. The instantaneous flame front and the contours of the rich and lean flammable limits, i.e., $(\bar{Z} + Z_{\square})$ = 0.091 and 0.026, which are estimated from the phase-averaged LIF data of the cold jet, are also depicted. The flammable mixture is distributed extensively in the radial direction at x/D_o > 1.5, just upstream of the flame base. Therefore, partially premixed flame is certainly dominant at the flame base, which is consistent with the observation of the blue chemiluminescent emission at the flame base. As shown in the velocity vector distribution, large-scale vortices are densely populated near the nozzle exit, which is very similar to the near-field structure of the cold jet (Fig. 6b). The leading edge flame at x/D_o ~ 1 is engulfed toward the jet axis by the fluid motion induced by the vortex. Since the location of the leading edge flame is fluctuating, the flame should be stabilized downstream as discussed below.

Axial variations of the velocity component $(\bar{u} + u_{\square})$ for the cold and flamed jet are shown in Fig. 11. The radial locations are r/D_o = 0, 0.39 and 0.75, which are respectively referred as A, B and C in Fig. 10. As shown in Fig. 11a, along the jet axis, the velocity of the flamed jet (= u_f) is in good agreement with that of the cold jet (= u_c) near the nozzle exit, while u_f becomes smaller than u_c at x/D_o > 1.7. It is conjectured that the decrease of u_f downstream is caused by the significant entrainment from the flame surrounding the jet axis. On the other hand, at r/D_o = 0.39, u_f is larger than u_c at x/D_o > 2 and the velocity difference $\Delta u = (u_f - u_c)$ continues to increase downstream. The velocity difference is likely to be caused by the thermal expansion across the flame front (Muniz-Mungal, 1997). Therefore, we assume that the phase-averaged flame is extended downstream of x/D_o ~ 2, which is consistent with the instantaneous thermal boundary as shown in Fig. 10. At r/D_o = 0.75, the flame front is assumed to be located at x/D_o = 1.2.

Figure 12 shows the phase-averaged velocity vectors $(\bar{u} + u_{\square})$ and the mixture fraction $(\bar{Z} + Z_{\square})$. Phase-averaged flame is defined as the region where the velocity difference increases as it goes downstream. Since partially premixed combustion is dominant at the flame base, the flame speed S_T propagating upstream balances with the local flow velocity. Assuming that S_T is constant over the flame base, S_T is estimated to be ~ 1.4 m/s, which is about four times of

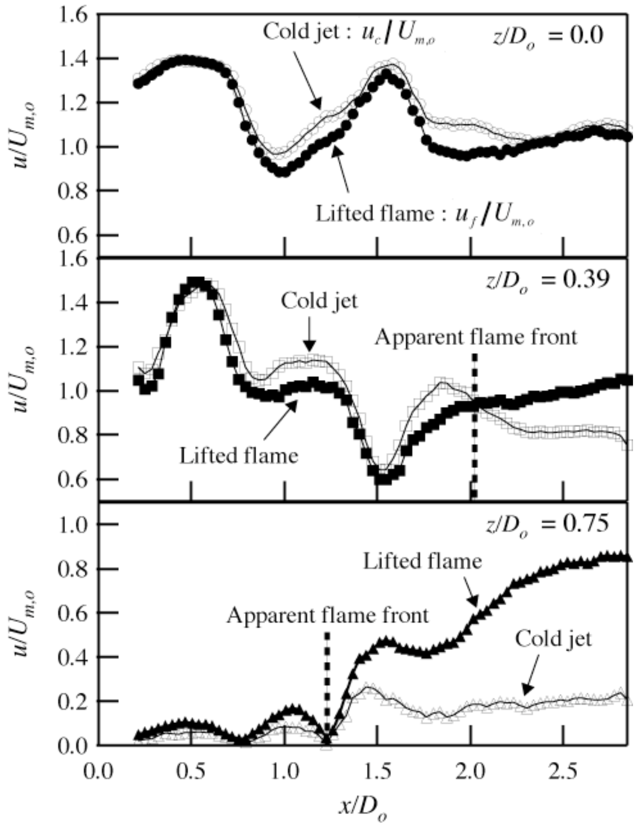

Fig. 11. Axial velocity variation of the controlled]lifted flame for the case 1 and the corr-esponding cold jet.

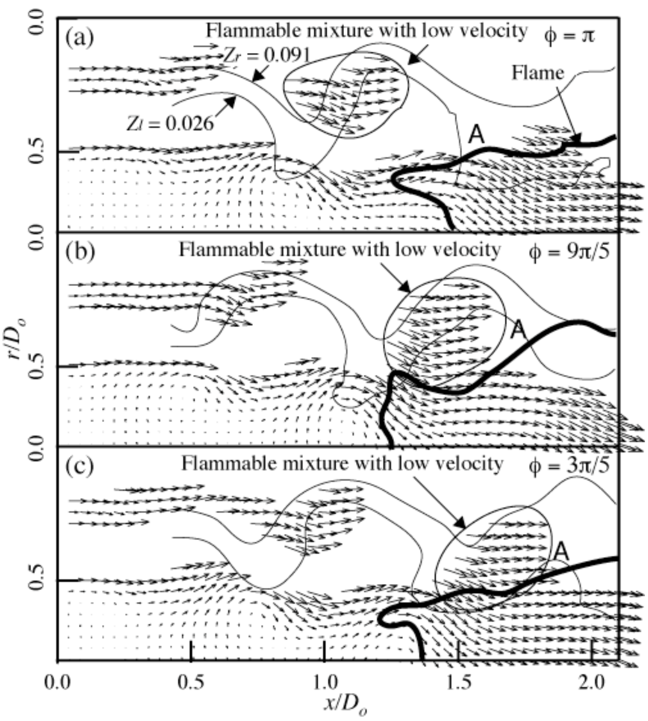

Fig. 12. Velocity vectors, $(\bar{u} + u_{\square})$, for the controlled lifted flame for the case 1. Velocity vectors smaller than S_T = 1.4 m/s are drawn. Contour of the velocity difference represents the flame. Flammable limits of the mixture fraction, $(\bar{Z} + Z_{\square})$, are also depicted.

the maximum laminar flame speed for methane. The velocity vectors smaller than S_T are overlaid in Fig. 12. As shown in Fig. 12a, the velocity at the flame base is smaller than S_T, while the velocity vectors right upstream of the flame base are larger than S_T, which implies that the estimation of S_T is reasonable.

It is found that the strong vortices induced by the flaps produce a blob of flammable mixture, of which velocity is smaller than the flame speed. The premixture blob is supplied to the flame base (A) at the flapping frequency. Since the dimension of the blob l_v is approximately $0.5D_o$ at the flame base, we defined the Damköhler number as the time ratio of the premixture supply and the consumption as follows:

$$D_a = \left(1/f_a\right)/\left(l_v/S_T\right), \tag{3}$$

The Damköhler number is 1.5, and thus $1/f_a$ approximately equals l_v/S_T. Therefore, the possible mechanism of the flame stabilization is that the time period of the premixture supply is balanced with the time necessary for the premixture to be burnt at the flame base.

4.4 Flame base structures for Case 2

Figure 13 shows a snap shot of the particle images and the velocity vectors $(\bar{u}_i + u_i')$ of Case 2. The instantaneous flame front and the contours of the rich and lean flammable limits are also depicted. It is found that small-scale vortices are dominant near the flame base and the flame front is not significantly disturbed by those vortices. The flammable mixture is distributed close to the jet axis due to the enhanced mixing upstream. This fact is in accordance with the conjecture that partially premixed combustion is dominant in the flame. Therefore, the flame speed should balance with the local flow velocity at the flame front. In the particle image, the mean and fluctuation of the liftoff height $\tilde{h}$ are depicted as $\bar{h}$ and $\sqrt{\overline{h'^2}}$, respectively. $\sqrt{\overline{h'^2}}$ is relatively small over all radial locations examined, implying that the flame is stable. This is because the velocity fluctuation at the flame base is relatively small, and the steady flame propagation is ensured.

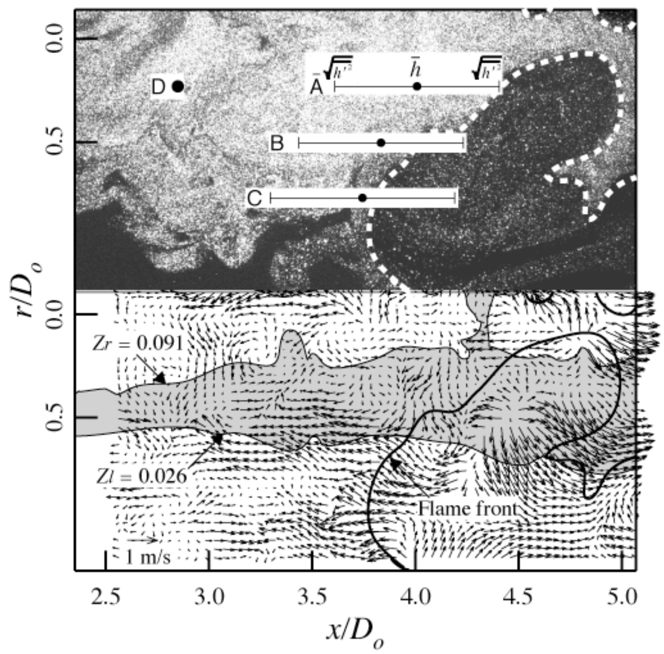

Fig. 13. Instantaneous particle images and the velocity, $(\bar{u}_i + u_i')$, for the controlled lifted flame in Case 2. Instantaneous thermal boundary and contours of the flammable limits in the mixture fraction, $(\bar{Z} + Z')$, are depicted in the figure.

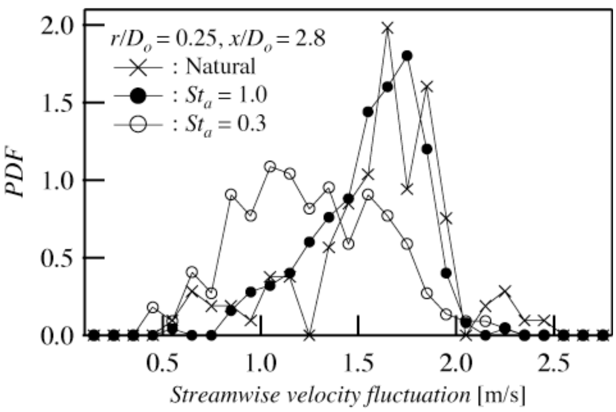

Fig. 14. PDF of the streamwise velocity fluctuation in the inner mixing layer at the upstream of the flame base.

Figure 14 shows the probability density function (PDF) of the streamwise velocity u_x in the inner mixing layer (point D in Fig. 13), which is obtained from 200 instantaneous PIV images. PDF in the natural and controlled cold jets with St_a = 0.3, where flames are unstable and easily blow off, are also depicted. In the unstable flames, there are a lot of peaks over a broad range of velocity. Thus, the large-scale vortical structures exists even at the flame base, and pass through the point intermittently with intense velocity fluctuations. It is conjectured that these periodic intense fluctuations prevent the steady flame propagation, and the flame easily blows off. On the other hand, in the controlled flame with St_a = 1.0, the PDF is distributed in a narrow range and has only one peak at u_x = 1.7 m/s. Therefore, the velocity fluctuations is less active at the flame base, which is consistent with the vortical structure shown in Fig. 13. Therefore, the flame stabilization mechanism in Case 2 is probably that the steady flame propagation is ensured at the flame base because of the absence of the large-scale vortices, which break down into turbulence upstream.

5. CONCLUSIONS

Active control of a lifted flame is investigated using a coaxial nozzle with miniature magnetic flap actuators arranged on the inner periphery of the annular nozzle. Through manipulation of the near-field vortical structures of coaxial jets, we can improve the flame stability and flexibly control the liftoff height. Spatio-temporal evolution of large-scale vortical structures are examined with the aid of PIV and LIF in order to elucidate the control mechanisms. It is found that the evolution of the outer shear layer is sensitive to the flap motion and the near-field vortical structures emerged in the shear layers play a dominant role in the flame stabilization.

By introducing the flap motion with the saw-wave signal, the outer shear layer is forced to roll up into strong large-scale vortices synchronized with the flap motion. When the flapping Strouhal number is unity, the lifted flame is anchored at $x/D_o \sim 1.5$ and becomes stable. The strong vortices induced by the flaps produce blobs of the flammable mixture which has the velocity smaller than the flame speed, and periodically supply them to the flame base. It is found that the time period of the premixture supply is balanced with the consumption time of the premixture.

On the other hand, when the jet is controlled by the flap motion with the square-wave signal, vortical structures emerged in the shear layers are relatively weak and break into turbulence near the nozzle exit. The lifted flame is located at $x/D_o \sim 4$, which is downstream of the inner potential core. At the flame base, the flame speed is balanced with the local flow velocity. The mechanism of the flame stabilization is that the upstream flame propagation is undisturbed due to the absence of large-scale vortices.

ACKNOWLEDGEMENT

This work was supported through the research project on ìMicro Gas Turbine/Fuel Cell Hybrid-Type Distributed Energy Systemî by the Department of Core Research for Evolutional Science and Technology (CREST) of the Japan Science and Technology Corporation (JST).

The present work also was supported in part through the 21st Century COE Program, “Mechanical Systems Innovation,” by the Ministry of Education, Culture, Sports, Science and Technology.

REFERENCE

ANSI/ASME PTC 19.1, “Measurement uncertainty,” supplement on instruments and apparatus, part 1, ASME.

Chao, Y. C. and Jeng, M. S., “Behavior of the lifted jet flame under acoustic excitation,” Twenty-fourth symp. (Int.) on Combst., (1992), pp. 333-340.

Chao, Y. C., Jong, Y. C. and Sheu, H. W., “Helical-mode excitaion of lifted flames using piezoelectric actuators”, Exp. Fluids, 28, (2000), pp. 11-20.

Dahm, W. J. A., Frieler, C. E. and Tryggvason, G., “Vortex structure and dynamics in the near field of a coaxial jet,” J. Fluid Mech., 241, (1992), pp. 371-402.

Gad-el-Hak, M., The MEMS Handbook, CRC PRESS, (2002), 35.

Hussain, A. K. M. F. and Zaman, K. B. M. Q., “The preferred mode of the axisymmetric mode”, J. Fluid Mech., 110, (1981), pp. 39-71.

Kean, R. D. and Adrian, R. J., “Optimization of particle image velocimeters. Part I: Double pulsed systems,” Meas. Sci. Technol., 1, (1990), pp. 1202-1215.

Kean, R. D. and Adrian, R. J., “Theory of cross-correlation analysis of PIV images,” J. Applied Scientific Research, 49, (1992), pp. 191-215.

Lozano, A., Yip, B. and Hanson, R. K., “Acetone: a tracer for concentration measurements in gaseous flows by planar laser-induced fluoreacence,” Exp. Fluids, 13, (1992), pp. 369-376.

Melling, A., “Tracer particles and seeding for particle image velocimetry,” Meas. Sci. Technol., 8, (1997), pp. 1406-1416.

Muniz, L. and Mungal, M. G., “Instantaneous flame-stabilization velocities in lifted-jet diffusion flames,” Comb. Flame, 111, (1997), pp. 16-31.

Peters, N. and Williams, F. A., “Liftoff characteristics of turbulent jet diffusion flames,” AIAA J., 21, (1983), pp. 423-429.

Pitts, W. M., “Assessment of Theories for The Behavior and Blowout of Lifted Turbulent Jet Diffusion Flames”, Twenty-second symp. (Int.) on Comb., (1988), pp. 809-816.

Rehab, H., Villermaux, E. and Hopfinger, E. J., “Flow regimes of large-velocity-ratio coaxial jets,” J. Fluid Mech., 345, (1997), pp. 357-381.

Suzuki, H., Suzuki, Y. and Kasagi, N., “Active control of an axisymmetric jet with distributed electromagnetic flap actuators,” Exp. Fluids, 36, (2004), pp. 498-509.

Vervisch, L., “Using numerics to help the understanding of non-premixed turbulent flames”, Proc. Combst. Inst., 28, (2000), pp. 11-24.

Vanquikenborne, L. and Trigglen, A. V., “The stabilization mechanism of lifted diffusion flames,” Combust. Flame, 10, (1966), pp. 59-69